DETC2022-89745

DISPERSION MORPHING IN HIGHLY-RECONFIGURABLE ROTATOR LATTICES

Lezheng Fang

Graduate Student
George W. Woodruff School of Mechanical
Engineering, Georgia Institute of Technology
Atlanta, GA 30332, USA
lezheng.fang@gatech.edu

Michael J. Leamy*

Professor School of Mechanical Engineering Georgia Institute of Technology Atlanta, GA 30332, USA michael.leamy@me.gatech.edu

ABSTRACT

We investigate wave propagation in in-plane rotator lattices demonstrate dispersion morphing and extreme acoustoelastic effects using analytical and numerical means. By changing the angle of the rotator arms attaching the elastic linkage between adjacent rotators, we show that the band structure may morph from a positive/negative-group-velocity passband into a flat band across the whole wavenumber space, and then into a negative/positive-group-velocity passband. A similar process can also occur at certain fixed arm angles when the lattice constant changes, which one may interpret as stretching or compressing the structure along the lattice directions, effectively mimicking the acoustoelastic effect. We analytically investigate both processes and provide closed-form expressions for the occurrence of flat bands, which indicates the transition of the passband property. Further, we explore a chiral rotator lattice design where the oscillation equilibrium position for each rotator may shift upon the change of the lattice constant. This design has a unique advantage that the morphed passband maintains approximately the same frequency range such that a signal may stay propagating during the process of dispersion morphing. In the end, we present numerical simulations for three potential applications utilizing the aforementioned findings. In these applications, both static and dynamic lattice stretching are considered, resulting in on-demand bi-directional wave-guiding, refraction bending, and time-modulated amplifying. Numerical simulations document a high-quality agreement with theory and yield promising results that may inspire next-generation reconfigurable metamaterials.

Keywords: rotator lattice, dispersion morphing, flat band, acoustoelastic effect, negative refraction, time modulation, parametric amplification.

1. INTRODUCTION

Periodic structures, a class of patterned structures with spatially repeated unit cells arranged in a lattice, continue to be an active area of research [1, 2]. In wave physics and engineering, periodic structures have advantageous features in on-demand wave guiding [3-5], focusing [6-8], imaging [9-12], sensing [13-16], protecting [17-19], and filtering [20-22]. Their spatially repeated patterns induce band structures that propagate and attenuate waves based on their frequency/energy [23]. Conventional designs typically engineer a specified band structure for a single purpose. Re-designs and fabrications are often required for other operating regimes or environments. In recent years, there has been an increasing demand for highly reconfigurable periodic structures, such that they adjust to diverse operating environments and are capable of tuning the desired features without excessive modification and extra costs.

In the field of elastic and acoustic periodic structures, researchers have adopted two primary approaches to design reconfigurable structures. The first approach utilizes programmed circuits and tunable electrical components, such as piezoelectric components, to achieve reconfigurable waveguiding [24, 25], multiplexing [26] and filtering [27, 28]. Despite their advantageous reconfigurability and tunability, the control systems associated with these structures may become significantly complicated and raise concerns about stability and energy consumption for many-degree-of-freedom systems. The second approach takes advantages of compliant structures, or switch-like structures, incorporating multi-stability and/or nonlinearity. In discrete structures, Nadkarni et al. [29] considered a set of bi-stable members connected by magnetic links and achieved tunable unidirectional wave guiding. Wu et al. [30] engineered a 1D metastable structure wherein the band structure can be reconfigured by shifting the magnet-spring equilibrium position. In acoustics, bandgaps are engineered by introducing geometric frustration [31] and axial deformation along a transmission line [32]. Very recently, Li *et al.* [33] studied a liquid-induced cellular microstructure transformation and assembly. These reconfigurable designs mostly avoid concerns with energy consumption and control stability; however, they only allow transitions between a finite (usually two) number of stable states.

Building on our previous work with rotator systems [34, 35], in this paper, we propose an analytical and numerical study of a class of mechanical in-plane rotator lattices that exhibit high reconfigurability with theoretically many stable states, and explore their potential applications. We show that in the proposed generalized rotator model, at a given lattice constant, the offset angle of the rotator arms affect the passband behavior. By reconfiguring this offset angle, the dispersion may morph from an acoustic type with positive group velocity, to an optical type with negative group velocity across the wavenumber space. At each offset angle, we observe different acoustoelastic effects. We also investigate a chiral-type rotator lattice by considering an asymmetric linkage between adjacent rotators, and observe a huge acoustoelastic effect associated with the equilibrium position shift. These results extend the space of possible rotator lattice applications.

2. GENERALIZIED IN-PLANE ROTATOR LATTICE

In our previous work [34], two types of rotator lattices, with different spring attaching locations, were introduced resulting in acoustic and optical dispersion, respectively, as shown in Fig. 1. The two types of connections, termed side-arm connection and nearest-arm connection, are indeed two special cases of a generalized rotator lattice model.

Introducing an offset angle θ_0 results in an angled connecting arm with respect to a normal line orthogonal to the lattice direction, as shown in the inscribed schematic in Fig. 2a. At a fixed normalized lattice constant, $\alpha = \frac{a}{r}$, the linearized equation of motion for each rotator under small-angle oscillation can be expressed as,

$$I\ddot{\theta}_{j} + (k_{1}\theta_{j} + k_{2}\theta_{j-1})\epsilon + (k_{1}\theta_{j} + k_{2}\theta_{j+1})\epsilon + O(\epsilon^{3}) = 0,$$
(1)

where j is the index of the studied rotator, and θ denotes the angular displacement. Parameters I, k_1 and k_2 represent the moment of inertia of the rotator and equivalent linear stiffness resulting from a Taylor expansion around the small-angle oscillation equilibrium ($\theta=0$ in this case). The stiffness terms are functions of spring parameters and geometry terms including normalized lattice constant α and offset angle θ_0 . The explicit forms of k_1 and k_2 are cumbersome and thus documented in the Appendix.

Applying the Bloch Theorem [36], we find the linear dispersion relation as,

$$\omega = \sqrt{\frac{1}{I}(2k_1 + 2k_2\cos\mu)},\tag{2}$$

where ω and μ denote the frequency and propagation constant, respectively. In Fig. 2a, we depict 10 dispersion curves corresponding to increasing offset angles. For visualization

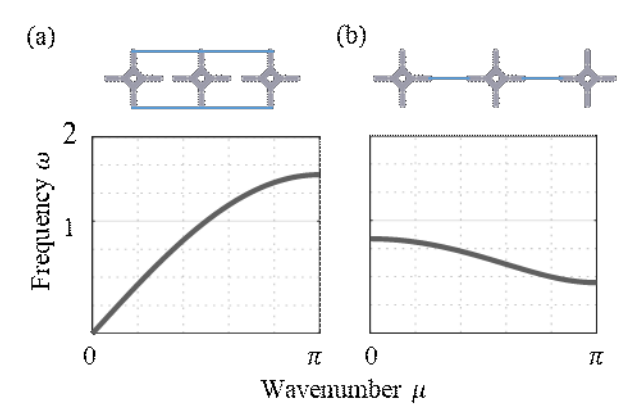


FIGURE 1: SCHEMATIC AND BAND STRUCTURE FOR TWO TYPES OF 1D-ROTATOR LATTICES. IN EACH CONFIGURATION, ROTATORS ARE PINNED AT THEIR CENTERS, WHICH ONLY SUPPORT ROTATIONAL MOTION. THE BLUE LINES DENOTE ELASTIC LINKAGES. (A) A ROTATOR CHAIN COUPLED FROM SIDE ARMS. (B) A ROTATOR CHAIN COUPLED FROM NEAREST ARMS.

convenience, we use the degree unit (°) instead of radian measure to describe all offset angles (and compromising angles in next section) in this work. Note that the $\theta_0=0^\circ$ and $\theta_0=90^\circ$ cases retrieve the solutions in Figs. 1a and 1b. We note that when the lattice constant is fixed, the offset angle determines the pattern of dispersion. As the offset angle increases, the passband morphs from an acoustic dispersion into an optical dispersion with negative group velocity. It indicates that a flat band across the entire Brillion zone occurs at the limit of the transition. We note that the critical offset angle corresponding to this flat band is challenging to express in an explicit form, but can be written in a much more elegant way from the lattice constant perspective discussed next.

At arbitrary fixed offset angle, the dispersion also shifts and morphs as the lattice constant (unit cell spacing) changes, which can be interpreted as an external stretch or compression along the lattice direction. In Fig. 2b we illustrate the dispersion morphing for three rotator lattices with $\theta_0=10^\circ,50^\circ$, and 90° by capturing the cut-on and cut-off frequencies at $\mu=0$ and $\mu=\pi$. As the unit cell spacing increases, both cut-on and cut-off frequencies increase, yet with non-identical rate and nonlinear trajectory. This phenomenon is robust for offset in the range of $\theta_0=(0,90^\circ]$. We note that the dispersion associated with $\theta_0=0$ is immune to the stretch. In the $\theta_0=50^\circ$ case (light blue), we observe the cut-on and cut-off frequencies cross each

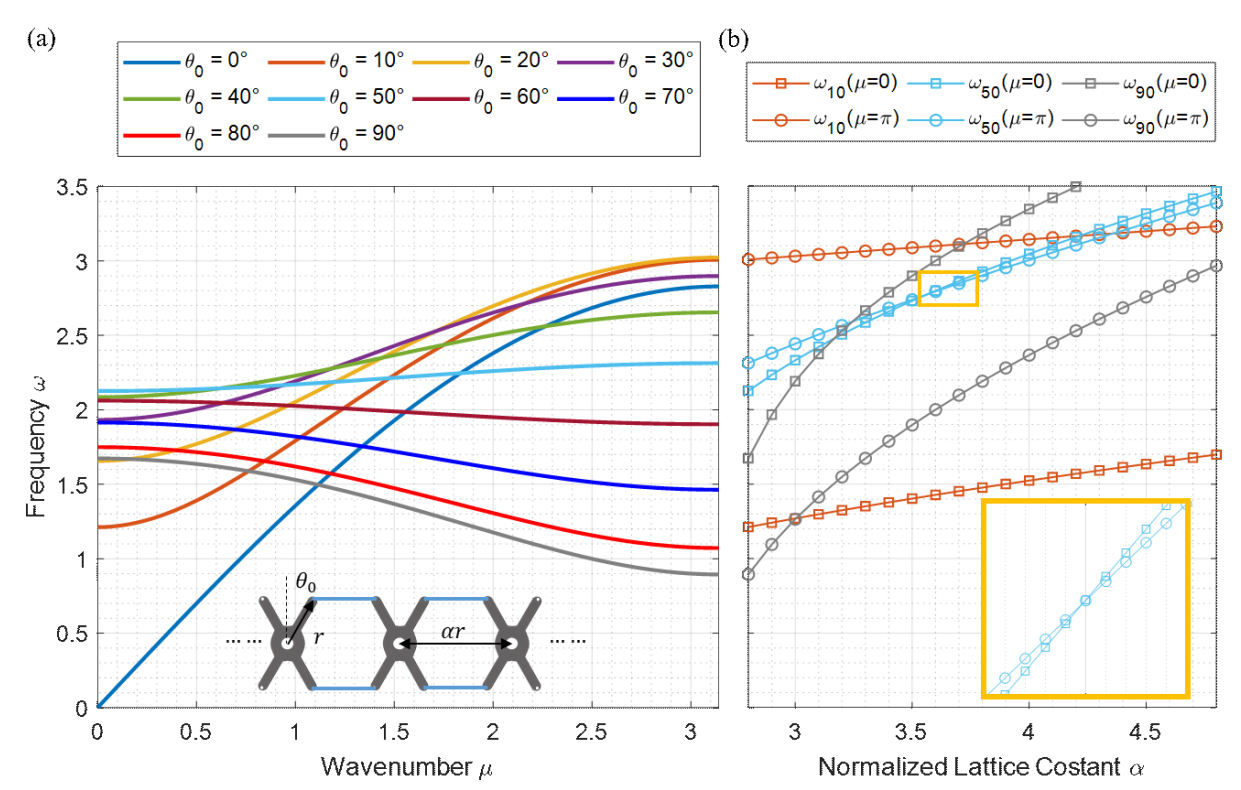


FIGURE 2: PARAMETRIC STUDY ON DISPERSION RELATION OF THE GENERALIZED ROTATOR LATTICE STRUCTURE. (A) THE DISPERSION CURVES ASSOCIATED WITH DIFFERENT OFFSET ANGLES. OFFSET ANGLES, RADIUS AND LATTICE CONSTANTS ARE MARKED ON THE EMBEDDED SCHEMATIC. (B) THE CUT-ON AND CUT-OFF FREQUENCIES AS A FUNCTION OF NORMALIZED LATTICE CONSTANT FOR THREE DIFFERENT OFFSET ANGLES. THE INSCRIBED PLOT ILLUSTRATES A CROSS OF THE CUT-ON AND CUT-OFF FREQUENCIES.

other in the process of stretching, as detailed in the zoomed-in view. The cross point illustrates a flat band as well as a transition of group velocity. At the flat band, frequency ω is independent of the wavenumber μ . This is equivalent to a zero k_2 in Eq. (2). Accordingly, a critical lattice constant inducing the flat band can be derived from the expression of k_2 (detailed in Appendix),

$$\alpha^* = \frac{\sin(\theta_0) (4r \sin^2(\theta_0) + L_0 \sin(\theta_0) + 2r)}{r(2 \sin^2(\theta_0) - 1)}$$
(3)

where L_0 is the undeformed length of the spring, and the offset angle θ_0 needs to be larger than 45°. For $\theta_0 < 45^\circ$, stretching the lattice will not induce a flat band. At the limit of $\theta_0 = 45^\circ$, the critical spacing is at infinity. An inverse function of Eq. (3) can be used to pursue the critical angle for the occurrence of a flat band at a fixed lattice constant, with the restriction of $\theta_0 > 45^\circ$.

3. CHIRAL ROTATOR LATTICE

By considering asymmetric elastic linkages between neighboring rotators, we introduce a variation of the discussed rotator lattices. As depicted in the schematic in Fig. 3a, each pair of neighboring rotators are only linked by one spring from their side arms instead of two, which lies on alternating sides of the rotator along the chain. We note that each rotator, along with its neighbor on each side, forms a pair of enantiomers, and hence we term this type of structure a chiral rotator lattice.

In the top configuration of the schematic in Fig. 3a, each elastic linkage is assumed pre-tensioned, and each rotator is subject to an additional torque from its base. This torque has a constant magnitude of $2k(\alpha_0r-L_0)r$, where k and α_0r denotes the spring stiffness and the lattice constant in the undeformed configuration (in the case, $\alpha_0=2.1$). The applied torques have identical magnitude but alternative directions for adjacent rotators, as indicated by the black arrows, and serve to stabilize the equilibrium position. Without these torques, the pretensioned springs offer unbalanced torques on each rotator and drive the lattice away from the current equilibrium. The equation of motion for each rotator is given as,

$$I\ddot{\theta}_{j} + K_{0} + (k_{1c}\theta_{j} + k_{2c}\theta_{j-1})\epsilon + (k_{1c}\theta_{j} + k_{2c}\theta_{j+1})\epsilon -T_{j} + O(\epsilon^{3}) = 0,$$
(4)

where k_{1c} and k_{2c} are equivalent stiffness terms (please see the Appendix for explicit expressions) similar to k_1 and k_2 in Eq. (1). In Eq. (4), the additional term K_0 denotes an unbalanced 0^{th} -order torque resulted from the asymmetric pretensioned springs, and T_j denotes the external constant torque with alternative directions to counteract this unbalanced term. At

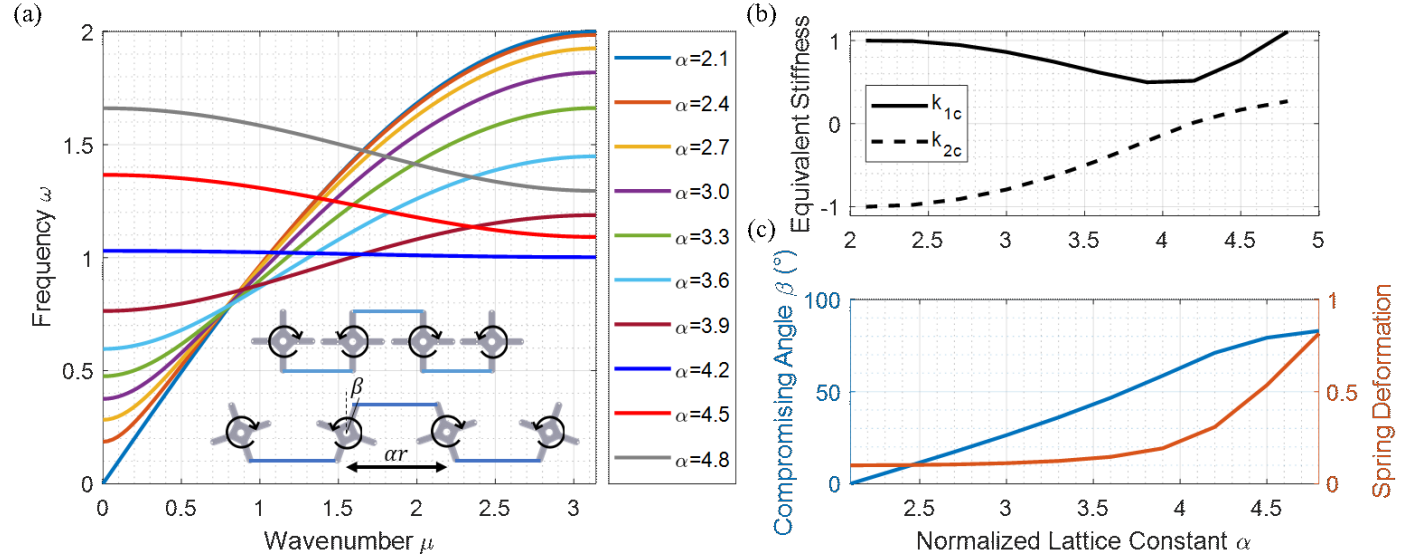


FIGURE 3: DISPERSION ANALYSIS ON A 1D CHIRAL ROTATOR STRUCTURE. (A) THE DISPERSION MORPHING WITH RESPECT TO THE CHANGE IN NORMALIZED LATTICE CONSTANT. THE EMBEDDED SCHEMATIC DESCRIBES THE COMPROMISING ANGLE AND LATTICE STRETCHING DYNAMICS. (B) THE EQUIVALENT STIFFNESS CHANGE IN THE PROCESS OF LATTICE STRETCHING. (C) THE EVOLUTION OF COMPROMISING ANGLE AND SPRING DEFORMATION IN THE PROCESS OF LATTICE STRETCHING.

the top configuration in Fig. 3a, where the side arms are held perpendicular to the lattice direction, we have $K_0 = T_i =$ $\pm 2k(\alpha_0 r - L_0)r$, and thus Eq. (4) can be written as,

$$I\ddot{\theta}_{j} + (k_{1c}\theta_{j} + k_{2c}\theta_{j-1})\epsilon + (k_{1c}\theta_{j} + k_{2c}\theta_{j+1})\epsilon + O(\epsilon^{3}) = 0,$$
which admits a similar form with Eq. (1).

When one attempts to apply a static stretch to the lattice along the lattice direction, as depicted in the lower configuration in Fig. 3a, the unit cell spacing changes, and the equilibrium position of each rotator shifts. This shift can be modeled by a compromising angle β as shown in the schematic, which relates to the external torque and unit cell spacing,

$$|T_i| = 2k\delta r\cos\beta\,,\tag{6}$$

$$\delta = \alpha r - L_0 - 2r \sin \beta \,. \tag{7}$$

 $\begin{aligned} \left|T_{j}\right| &= 2k\delta r\cos\beta\,, \\ \delta &= \alpha r - L_{0} - 2r\sin\beta\,, \end{aligned} \tag{6}$ where δ denotes the spring deformation. Note that in this equation, $|T_i|$ is constant and β is a function of normalized spacing α . At each spacing, the equation of motion of a chiral rotator admits an identical form as in Eq. (5), however with a shifted equilibrium position,

$$I\ddot{\hat{\theta}}_{j} + \left(k_{1c}\hat{\theta}_{j} + k_{2c}\hat{\theta}_{j-1}\right)\epsilon + \left(k_{1c}\hat{\theta}_{j} + k_{2c}\hat{\theta}_{j+1}\right)\epsilon + O(\epsilon^{3}) = 0, \tag{8}$$
where $\hat{\theta}_{j+2n} = \theta_{j+2n} + \beta, \hat{\theta}_{j+2n-1} = \theta_{j+2n-1} - \beta$, and $n \in \mathbf{Z}$.
Accordingly, we compute and plot the dispersion at each

spacing in Fig. 3a, and illustrate the compromising angles as well as the spring deformations in Fig. 3c. We observe that when we stretch the lattice (in a static way), the dispersion morphs from an acoustic branch into optical branches with positive group velocity, then a flat band, and eventually a negative-group velocity band. Different from that shown in Fig. 2b, the cut-on and cut-off frequencies in Fig. 3a do not experience monotonic

increases, and the passband maintains approximately the same frequency range, until the stretch grows excessively large (the last two dispersion curves shift upwards considerably). This observation can be explained by the lattice stretching process detailed in Figs. 3b and 3c. When the unit cell spacing first starts to increase, the change in the compromising angle is more dramatic than the change of the spring deformation. In this phase, one of the equivalent stiffness decreases and the other increases in Fig. 3b. Reflected on the band structure in Fig. 3a, the dispersion pattern morphs, yet stays around the same frequency range. When the compromising angle approaches 90° in Fig. 3c, its increase slows, and the lattice stretch now mostly translates to the stretch on the springs, which raises up both equivalent stiffness terms in Fig. 3b. Accordingly, the dispersion curves shift upwards across the whole Brillouin zone (see the last two dispersion curves).

To conclude, an advantageous feature of the chiral type rotator lattice is its capability of morphing the pattern of the passband without excessively shifting it in the process of lattice stretching. In the following two sections, we will introduce three rotator lattice structures and apply the dispersion morphing theory, as well as verify the theory using numerical simulations.

4. APPLICATIONS - STATIC LATTICE STRETCH

In this section, we explore two applications stemming from the analytical findings in the rotator lattice. Both applications extend the theory to 2D rotator structures and stretch them statically along the lattice direction. The first application achieves a bi-directional wave-guiding phenomenon whereby external stretches can be used to guide waves propagating mostly perpendicular to the stretch direction. The second application exhibits a reconfigurable refractive index, and a signal may

choose to refract to the same side or the other side of the interface normal based on external stretches. The wave dynamics are simulated by numerically integrating the equations of motion using MATLAB's ODE45 function.

The first structure, as shown in Fig. 4, depicts a non-chiral 2D rotator lattice with offset angle $\theta_0 = 45^{\circ}$. A singlefrequency harmonic force excites the lattice at the center. By stretching the lattice either vertically (Fig. 4b) or horizontally (Fig. 4c), we morph the dispersion for desired anisotropy and the associated directional wave-guiding. As shown in the numerical simulation in Fig. 4b, at the given frequency ($\omega = 5$), a vertically-stretched lattice propagates most of the wave energy horizontally, which agrees with the group velocity contour analytically computed [36]. Similarly, if a lattice is stretched horizontally by the same amount, the wave shall propagate mostly in the vertical direction, as shown the Fig. 4c. We note that the shown directivity is not a narrowband phenomenon given the anisotropic lattice, a wide range of frequencies within the passband can induce similar group velocity patterns, which leads to directional energy flow.

The second structure, as shown in Fig. 5, constructs an interface problem between a chiral and non-chiral rotator structure whose passbands partially overlap. The top media adopts a chiral rotator structure as shown in Fig. 5a, and the bottom media adopts a non-chiral rotator lattice with zero offset

angle. We note that the band structure of a zero-offset rotator lattice is immune to stretch along the lattice directions. The lattice is excited by an oblique incident wave starting from the bottom left corner.

In Figs. 5a-c, the lattice is not stretched. The band structure of two media are designed to be identical, as depicted in Fig. 5b, such that the transmission is full (Fig. 5c). When we introduce a large bi-directional stretch, the unit cell rotates to its new equilibrium position shown in Fig. 5d, and its dispersion morphs into an optical branch with negative group velocity across the Brillouin zone, illustrated by the red curve in Fig. 5e. Accordingly, a negative refraction occurs at the interface [34]. We note that the lattice stretch process is reversible due to the existence of external torques discussed in the last section.

These two structures illustrate highly reconfigurable anisotropic properties and refractive index, which play important roles in directional energy transfer and information transport, and can relate to acoustic multiplexing and demultiplexing [26]. Additionally, the reverse design of these structures can be utilized to sense global and local deformation based on the wave propagation pattern.

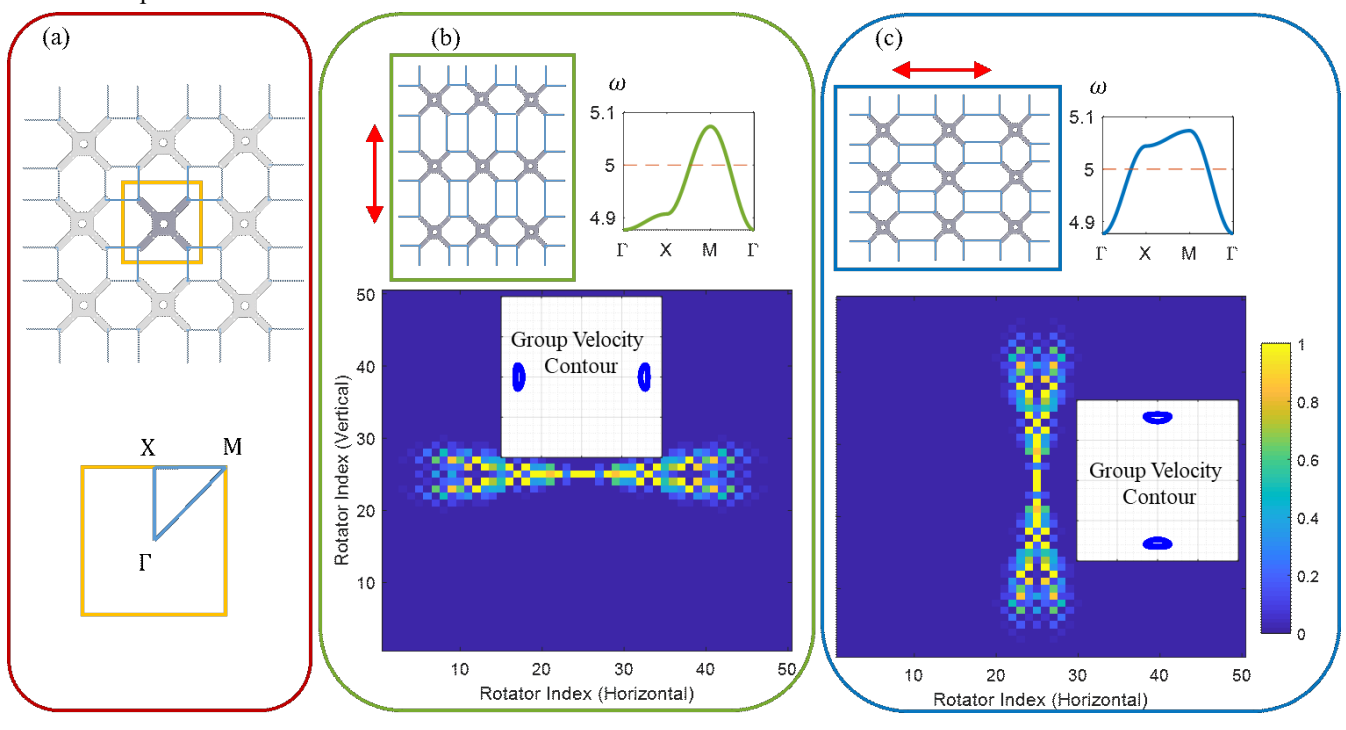


FIGURE 4: APPLICATIONS – BI-DIRECTIONAL WAVE-GUIDING. (A) SCHEMATIC OF THE ROTATOR LATTICE WITH UNIT CELL DEFINED. (B) AND (C) THE VERTICALLY AND HORIZONTALLY STRETCHED LATTICE. THE BAND STRUCTURE IS PLOTTED AS A SUBPLOT WITH THE RED DASHED LINE INDICATING THE EXCITATION FREQUENCY. THE COLOR FIELDS DESCRIBE THE SPATIAL DISTRIBUTION OF ENERGY IN THE PROCESS OF WAVE PROPAGATION. EACH PIXEL REPRESENTS A SINGLE ROTATOR. GROUP VELOCITY CONTOURS AT THE EXCITATION FREQUENCY ARE PROVIDED, WITH HORIZONTAL AND VERTICAL AXES DENOTE HORIZONTAL AND VERTICAL COMPONENT OF GROUP VELOCITY. FOR BOTH AXES, THE CONTOUR IS CENTERED AT ZERO.

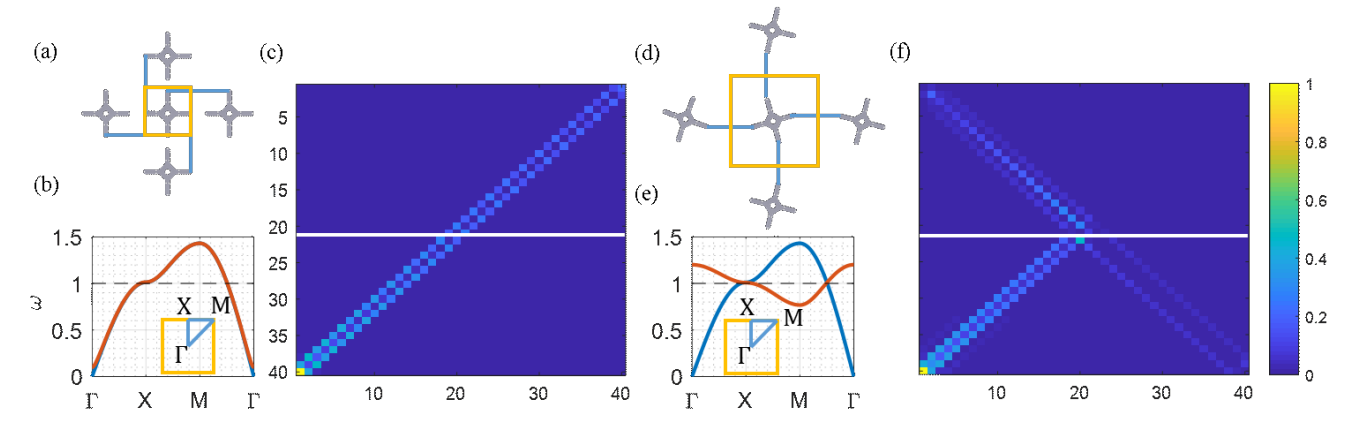


FIGURE 5: APPLICATIONS – TUNABLE REFRACTION. (A) THE SCHEMATIC OF AN UN-DEFORMED CHIRAL ROTATOR LATTICE. (B) THE BAND STRUCTURE OF THE CONFIGURATION IN (A). THE RED AND BLUE CURVES DENOTE THE DISPERSION CURVES FOR THE TOP AND BOTTOM MEDIA. (C) THE SIMULATED WAVE PROPAGATION PROFILE, WITH THE WHITE LINE INDICATING THE INTERFACE. (D) THE SCHEMATIC OF A DEFORMED CHIRAL ROTATOR LATTICE. (E) THE DISPERSION OF DEPICTED CONFIGURATION IN (D). (F) THE WAVE PROPAGATION PROFILE ASSOCIATED WITH A DEFORMED CHIRAL ROTATOR LATTICE.

5. APPLICATIONS - DYNAMIC LATTICE STRETCH

In this section, we introduce a 1D non-chiral rotator chain with an offset angle $\theta_0 = 90^\circ$ and time-modulated unit cell spacing. As shown in Fig. 6a, the spacing between each pair of unit cells fluctuates in time with an amplitude λ_m and frequency ω_m . To derive the modulated dispersion relation, we adopt the approach in [27, 37], and assume a linearized solution of the form,

$$\theta_j(t) = e^{i(\omega t - \mu j)} \sum_{n = -\infty}^{+\infty} \hat{\theta}_n e^{in\omega_m t}$$
 (9)

where $\hat{\theta}_n$ is the coefficient of the Fourier-expanded solutions. By inserting Eq. (9) into Eq. (1), we solve a quadratic eigenvalue problem in terms of ω at each normalized wavenumber $\mu \in [0,\pi]$. In Fig. 6b, we present the resultant band structures. Note that the blue and red curves represent dispersion curves corresponding to real (left y-axis) and imaginary frequency (right y-axis), respectively. We make three observations for the modulated dispersion in Fig. 6b.

- When two branches meet, they merge and form a flat band with complex frequency.
- The flat bands locate at $\frac{\omega_m}{2}$, and can be shifted along this frequency by varying the modulation frequency.
- The flat band can be broadened by increasing the modulation amplitude λ_m . In this process, the magnitude of the imaginary frequency also increases.

Due to the presence of imaginary frequency, a signal excited at the flat band shall grow exponentially in time if no energy dissipation is applied. Hence, this time-modulated system is capable of amplifying a specific frequency out of a broadband excitation. We model such a scenario in numerical simulations. Using numerical simulations, we send a finite pulse whose frequency content is centered around $\omega=1.25~rad/s$, as described in Fig. 6c. We then perform a 2D Fast Fourier Transformation (FFT) on the response to investigate the propagated frequency and wavenumber. To avoid unbounded amplitudes, we introduce viscous damping into the system and ensure the wave amplitudes are small. In Figs. 6d and 6e, we superimpose the two dispersions highlighted in Fig. 6b on the associated numerical FFT results. Specifically, Fig. 6d, with the orange frame, is compared with the bottom left configuration in Fig. 6b, and Fig. 6e, with the green frame, is compared with the top-right configuration in Fig. 6b. We observe that the numerical FFT results peak at a frequency-wavenumber pair on the flat band where the imaginary frequency is maximized, which agrees with the theory.

The flat band observations and parametric amplifications are consistent with previous studies [38]. However, this system is rather unique since the modulation applies on a geometric parameter – the unit cell spacing in a macro scale. Thus, a reverse engineering of such can apply to motion sensing, where the location of a flat band deciphers the amplitude and frequency of the motion modulating the lattice.

6. CONCLUSIONS

The proposed study investigates two types of reconfigurable in-plane rotator lattices and associated reversible dispersion morphing phenomenon. Two key parameters, offset angle and unit cell spacing, are specifically studied to illustrate their effect on the band structures of the rotator lattices. The dispersion morphing resulting from the change of unit cell spacing is analogous to an acoustoelastic effect. In the generalized rotator lattice, a change in either key parameter is capable of converting the passband from a positive-group-velocity branch to a flat band, and then a negative-group-velocity branch. For the chiral rotator lattice, an increasing unit cell spacing morphs an acoustic

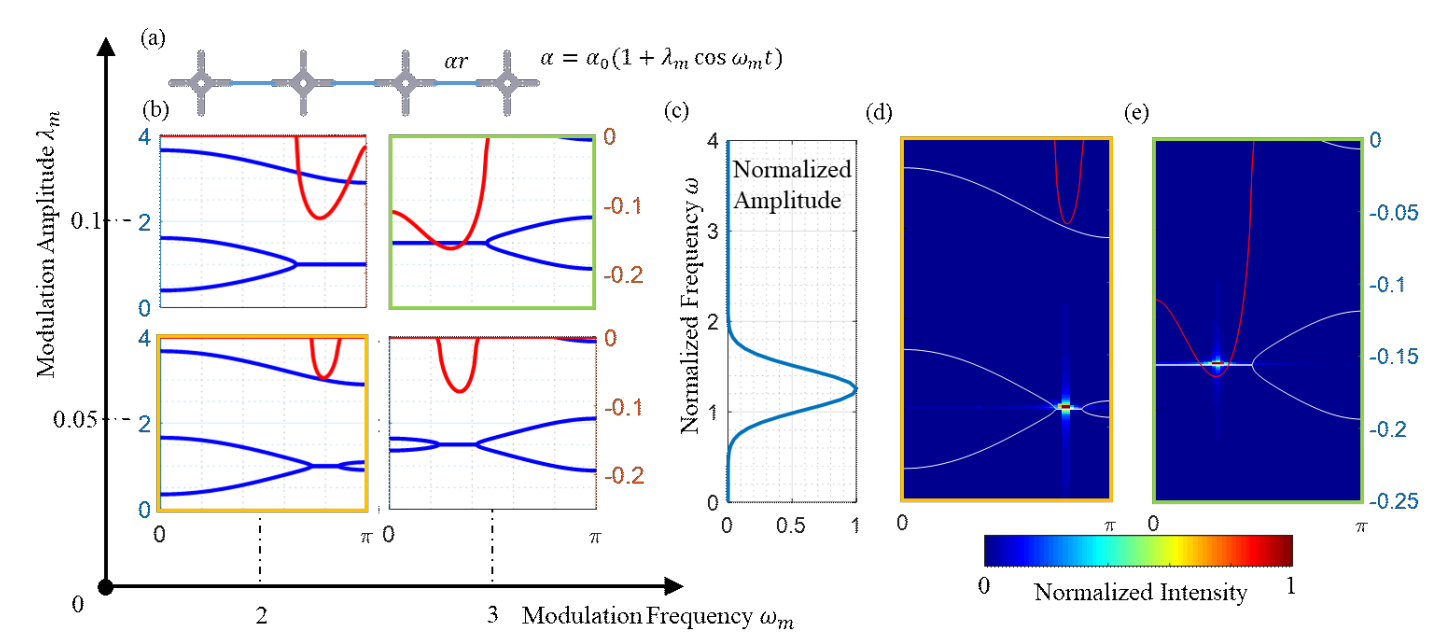


FIGURE 6: APPLICATIONS – TIME-MODULATED LATTICE. (A) THE SCHEMATIC OF A 1D ROTATOR LATTICE WITH UNIT CELL SPACING MODULATED IN TIME. (B) FOUR DISPERSION RELATIONS CORRESPONDING TO DIFFERENT MODULATION AMPLITUDE AND FREQUENCY. THE HORIZONTAL AND VERTICAL AXES ARE WAVENUMBER AND FREQUENCY, RESPECTIVELY. (C) THE FREQUENCY CONTENT OF A TESTING SIGNAL IN NUMERICAL SIMULATIONS. (D) AND (E) THE NUMERICAL RESULTS WITH MODULATION PARAMETERS HIGHLIGHTED IN (B). THE RESULTS ARE COMPARED TO CORRESPONDING ANALYTICAL BAND STRUCTURES.

branch into an optical branch without shifting it to higher frequency.

We also explore applications of the 1D and 2D rotator lattices under static or dynamic stretching. A bi-directional waveguide is numerically validated in an offset non-chiral rotator lattice. The chiral structure interfaced with a non-chiral lattice with zero offset angle illustrates tunable refraction index when subject to bi-directional stretch. Finally, a time-modulated

ACKNOWLEDGMENTS

The authors would like to thank the National Science Foundation for support of this research under an Emerging Frontiers in Research and Innovation (EFRI) Grant No. 1741565.

APPENDIX - EQUIVALENT STIFFNESS

In Eq. (1), the equivalent stiffness k_1 and k_2 have expression,

lattice demonstrates the emergence of flat bands and associated parametric amplification in a rotator lattice, which can be applied to motion sensing. The theory and applications presented may inspire future reconfigurable metamaterial designs. Follow-on research will include experimental validation and investigation of dissipation and nonlinear effects in consideration of practical implementation.

$$\begin{split} & \frac{1}{\left(\alpha^{2} - 4\sin(\theta_{0})\alpha - 4\cos(\theta_{0})^{2} + 4\right)^{5/2}} \left(2kr\left(\left(32\cos(\theta_{0})^{6} + \left(80\sin(\theta_{0})\alpha\right)\alpha\right) - 24\alpha^{2} - 80\right)\cos(\theta_{0})^{4} + \left(56\alpha^{2}\sin(\theta_{0})^{2} - 40\left(\alpha^{2} + \frac{16}{5}\right)\alpha\sin(\theta_{0}) + 6\alpha^{4} + 48\alpha^{2} + 64\right)\cos(\theta_{0})^{2} + \left(\alpha^{2} - 4\sin(\theta_{0})\alpha + 4\right)\left(\alpha\left(\alpha^{2} + 8\right)\sin(\theta_{0}) - 5\alpha^{2} - 4\right)\right) \\ & r\sqrt{\alpha^{2} - 4\sin(\theta_{0})\alpha - 4\cos(\theta_{0})^{2} + 4} - \left(16\cos(\theta_{0})^{6} + \left(48\sin(\theta_{0})\alpha - 56\alpha^{2} - 48\right)\cos(\theta_{0})^{4} + \left(-32(\alpha^{2} + 3)\alpha\sin(\theta_{0}) + 9\alpha^{4} + 112\alpha^{2} + 48\right)\cos(\theta_{0})^{2} + \left(\alpha^{4} + 32\alpha^{2} + 48\right)\alpha\sin(\theta_{0}) - 9\alpha^{4} - 56\alpha^{2} - 16\right)L_{0}) \end{split}$$

$$\begin{split} & \frac{1}{\left(\alpha^{2} - 4\sin(\theta_{0})\alpha - 4\cos(\theta_{0})^{2} + 4\right)^{5/2}} \left(2kr\left(\left(-32\cos(\theta_{0})^{6} + \left(-64\sin(\theta_{0})\alpha\right)\alpha + 8\alpha^{2} + 80\right)\cos(\theta_{0})^{4} + \left(-40\alpha^{2}\sin(\theta_{0})^{2} - 40\left(-\frac{2\alpha^{2}}{5} - \frac{12}{5}\right)\alpha\sin(\theta_{0}) - 2\alpha^{4} - 16\alpha^{2} - 64\right)\cos(\theta_{0})^{2} + \left(\alpha^{2} - 4\sin(\theta_{0})\alpha + 4\right)^{2}\right) \\ & r\sqrt{\alpha^{2} - 4\sin(\theta_{0})\alpha - 4\cos(\theta_{0})^{2} + 4} - \left(-16\cos(\theta_{0})^{6} + \left(-32\sin(\theta_{0})\alpha + 24\alpha^{2} + 48\right)\cos(\theta_{0})^{4} + \left(-32\left(-\frac{\alpha^{2}}{4} - 2\right)\alpha\sin(\theta_{0}) - \alpha^{4} - 48\alpha^{2} - 48\right)\cos(\theta_{0})^{2} + \left(-8\alpha^{2} - 32\right)\alpha\sin(\theta_{0}) + \alpha^{4} + 24\alpha^{2} + 16\right)L_{0}\right) \end{split}$$

In Eq. (4), the equivalent stiffness k_{1c} and k_{2c} are functions of β instead of θ_0 . Their expressions are very similar to those of k_1 and k_2 . The explicit expressions are given as,

$$\begin{split} & k_{1c} = \\ & \frac{1}{\left(\alpha^2 - 4\sin(\beta) \alpha - 4\cos(\beta)^2 + 4\right)^{5/2}} \left(rk \left(r \left(32\cos(\beta)^6 + \left(80\sin(\beta) \alpha - 16\alpha^2 + 80 \right) \cos(\beta)^4 + \left(64\alpha^2 \sin(\beta)^2 - 40 \left(\alpha^2 + \frac{16}{5} \right) \alpha \sin(\beta) + 6\alpha^4 + 40\alpha^2 \right) \right) \\ & + 64 \left(\cos(\beta)^2 + \left(\alpha^2 - 4\sin(\beta) \alpha + 4 \right) \left(\alpha \left(\alpha^2 + 8 \right) \sin(\beta) - 5\alpha^2 - 4 \right) \right) \\ & \sqrt{\alpha^2 - 4\sin(\beta) \alpha - 4\cos(\beta)^2 + 4} - L_0 \left(16\cos(\beta)^6 + \left(48\sin(\beta) \alpha - 56\alpha^2 \right) \right) \\ & - 48 \left(\cos(\beta)^4 + \left(-32\left(\alpha^2 + 3 \right) \alpha \sin(\beta) + 9\alpha^4 + 112\alpha^2 + 48 \right) \cos(\beta)^2 + \left(\alpha^4 + 32\alpha^2 + 48 \right) \alpha \sin(\beta) - 9\alpha^4 - 56\alpha^2 - 16 \right)) \end{split}$$

$$\begin{split} &\frac{1}{\left(\alpha^{2}-4\sin(\beta)\alpha-4\cos(\beta)^{2}+4\right)^{5/2}} \left(rk\left(r\left(-32\cos(\beta)^{6}+\left(-64\sin(\beta)\alpha+80\right)\cos(\beta)^{4}+\left(-48\alpha^{2}\sin(\beta)^{2}-40\left(-\frac{2\alpha^{2}}{5}-\frac{12}{5}\right)\alpha\sin(\beta)-2\alpha^{4}-8\alpha^{2}\right)\right) \\ &+80)\cos(\beta)^{4}+\left(-48\alpha^{2}\sin(\beta)^{2}-40\left(-\frac{2\alpha^{2}}{5}-\frac{12}{5}\right)\alpha\sin(\beta)-2\alpha^{4}-8\alpha^{2}\right) \\ &-64\left(\cos(\beta)^{2}+\left(\alpha^{2}-4\sin(\beta)\alpha+4\right)^{2}\right)\sqrt{\alpha^{2}-4\sin(\beta)\alpha-4\cos(\beta)^{2}+4}-L_{0}\left(-\frac{\alpha^{2}}{4}-2\right)\alpha\sin(\beta)\right) \\ &-16\cos(\beta)^{6}+\left(-32\sin(\beta)\alpha+24\alpha^{2}+48\right)\cos(\beta)^{4}+\left(-32\left(-\frac{\alpha^{2}}{4}-2\right)\alpha\sin(\beta)\right) \end{split}$$

$$\left. -\alpha^4 - 48\,\alpha^2 - 48\right) \cos(\beta)^2 + \left(-8\,\alpha^2 - 32\right)\alpha\sin(\beta) + \alpha^4 + 24\,\alpha^2 + 16\right) \bigg] \bigg)$$

REFERENCES

 $k_{2c} =$

- [1] Engheta, N., and Ziolkowski, R. W., 2006, Metamaterials: physics and engineering explorations, John Wiley & Sons.
- [2] Elachi, C., 1976, "Waves in active and passive periodic structures: A review," Proceedings of the IEEE, 64(12), pp. 1666-1698.
- [3] Kim, S.-H., and Das, M. P., 2012, "Seismic waveguide of metamaterials," Modern Physics Letters B, 26(17), p. 1250105.
- [4] Bock, P. J., Cheben, P., Schmid, J. H., Lapointe, J., Delâge, A., Janz, S., Aers, G. C., Xu, D.-X., Densmore, A., and Hall, T.

- J., 2010, "Subwavelength grating periodic structures in siliconon-insulator: a new type of microphotonic waveguide," Optics express, 18(19), pp. 20251-20262.
- [5] Halir, R., Bock, P. J., Cheben, P., Ortega Moñux, A., Alonso Ramos, C., Schmid, J. H., Lapointe, J., Xu, D. X., Wangüemert Pérez, J. G., and Molina Fernández, Í., 2015, "Waveguide sub wavelength structures: a review of principles and applications," Laser & Photonics Reviews, 9(1), pp. 25-49. [6] Guenneau, S., Movchan, A., Pétursson, G., and Ramakrishna, S. A., 2007, "Acoustic metamaterials for sound focusing and confinement," New Journal of physics, 9(11), p. 399.
- [7] Fang, A., Koschny, T., and Soukoulis, C. M., 2009, "Optical anisotropic metamaterials: Negative refraction and focusing," Physical Review B, 79(24), p. 245127.
- [8] Eleftheriades, G. V., and Siddiqui, O. F., 2005, "Negative refraction and focusing in hyperbolic transmission-line periodic grids," IEEE transactions on microwave theory and techniques, 53(1), pp. 396-403.
- [9] Fang, N., and Zhang, X., "Imaging properties of a metamaterial superlens," Proc. Proceedings of the 2nd IEEE Conference on Nanotechnology, IEEE, pp. 225-228.
- [10] Watts, C. M., Shrekenhamer, D., Montoya, J., Lipworth, G., Hunt, J., Sleasman, T., Krishna, S., Smith, D. R., and Padilla, W. J., 2014, "Terahertz compressive imaging with metamaterial spatial light modulators," Nature Photonics, 8(8), pp. 605-609.
- [11] Hunt, J., Driscoll, T., Mrozack, A., Lipworth, G., Reynolds, M., Brady, D., and Smith, D. R., 2013, "Metamaterial apertures for computational imaging," Science, 339(6117), pp. 310-313.
- [12] Dammann, H., and Klotz, E., 1977, "Coherent optical generation and inspection of two-dimensional periodic structures," Optica Acta: International Journal of Optics, 24(4), pp. 505-515.
- [13] Xu, W., Xie, L., and Ying, Y., 2017, "Mechanisms and applications of terahertz metamaterial sensing: a review," Nanoscale, 9(37), pp. 13864-13878.
- [14] Chen, T., Li, S., and Sun, H., 2012, "Metamaterials application in sensing," Sensors, 12(3), pp. 2742-2765.
- [15] Baz, A., 2001, "Active control of periodic structures," J. Vib. Acoust., 123(4), pp. 472-479.
- [16] Byford, J. A., Park, K. Y., and Chahal, P., "Metamaterial inspired periodic structure used for microfluidic sensing," Proc. 2015 IEEE 65th Electronic Components and Technology Conference (ECTC), IEEE, pp. 1997-2002.
- [17] Jiang, Z. H., Yun, S., Toor, F., Werner, D. H., and Mayer, T. S., 2011, "Conformal dual-band near-perfectly absorbing mid-infrared metamaterial coating," ACS nano, 5(6), pp. 4641-4647.
- [18] Yang, Y., Gao, Z., Xue, H., Zhang, L., He, M., Yang, Z., Singh, R., Chong, Y., Zhang, B., and Chen, H., 2019, "Realization of a three-dimensional photonic topological insulator," Nature, 565(7741), pp. 622-626.
- [19] He, C., Ni, X., Ge, H., Sun, X.-C., Chen, Y.-B., Lu, M.-H., Liu, X.-P., and Chen, Y.-F., 2016, "Acoustic topological insulator and robust one-way sound transport," Nature physics, 12(12), pp. 1124-1129.

- [20] Gil, M., Bonache, J., and Martin, F., 2008, "Metamaterial filters: A review," Metamaterials, 2(4), pp. 186-197.
- [21] Zhu, H., and Semperlotti, F., 2013, "Metamaterial based embedded acoustic filters for structural applications," AIP Advances, 3(9), p. 092121.
- [22] Barbarosie, C., and Neves, M., 2004, "Periodic structures for frequency filtering: analysis and optimization," Computers & structures, 82(17-19), pp. 1399-1403.
- [23] Kittel, C., 2021, "Introduction to solid state physics Eighth edition."
- [24] Casadei, F., Delpero, T., Bergamini, A., Ermanni, P., and Ruzzene, M., 2012, "Piezoelectric resonator arrays for tunable acoustic waveguides and metamaterials," Journal of Applied Physics, 112(6), p. 064902.
- [25] Darabi, A., Ni, X., Leamy, M., and Alù, A., 2020, "Reconfigurable Floquet elastodynamic topological insulator based on synthetic angular momentum bias," Science advances, 6(29), p. eaba8656.
- [26] Darabi, A., Kliewer, E., and Leamy, M. J., 2021, "Reconfigurable acoustic multiplexer/demultiplexer using time division," Applied Physics Letters, 119(11), p. 113501.
- [27] Trainiti, G., Xia, Y., Marconi, J., Cazzulani, G., Erturk, A., and Ruzzene, M., 2019, "Time-periodic stiffness modulation in elastic metamaterials for selective wave filtering: Theory and experiment," Physical review letters, 122(12), p. 124301.
- [28] Xu, X., Wu, Q., Chen, H., Nassar, H., Chen, Y., Norris, A., Haberman, M. R., and Huang, G., 2020, "Physical observation of a robust acoustic pumping in waveguides with dynamic boundary," Physical review letters, 125(25), p. 253901.
- [29] Nadkarni, N., Arrieta, A. F., Chong, C., Kochmann, D. M., and Daraio, C., 2016, "Unidirectional transition waves in bistable lattices," Physical review letters, 116(24), p. 244501.

- [30] Wu, Z., Zheng, Y., and Wang, K., 2018, "Metastable modular metastructures for on-demand reconfiguration of band structures and nonreciprocal wave propagation," Physical Review E, 97(2), p. 022209.
- [31] Wang, P., Zheng, Y., Fernandes, M. C., Sun, Y., Xu, K., Sun, S., Kang, S. H., Tournat, V., and Bertoldi, K., 2017, "Harnessing geometric frustration to form band gaps in acoustic channel lattices," Physical Review Letters, 118(8), p. 084302.
- [32] Babaee, S., Viard, N., Wang, P., Fang, N. X., and Bertoldi, K., 2016, "Harnessing deformation to switch on and off the propagation of sound," Advanced Materials, 28(8), pp. 1631-1635.
- [33] Li, S., Deng, B., Grinthal, A., Schneider-Yamamura, A., Kang, J., Martens, R. S., Zhang, C. T., Li, J., Yu, S., and Bertoldi, K., 2021, "Liquid-induced topological transformations of cellular microstructures," Nature, 592(7854), pp. 386-391.
- [34] Fang, L., and Leamy, M. J., "Negative Refractive Index in a Two-Dimensional Nonlinear Rotator Lattice," Proc. International Design Engineering Technical Conferences and Computers and Information in Engineering Conference, American Society of Mechanical Engineers, p. V010T010A002. [35] Fang, L., Mojahed, A., Darabi, A., Vakakis, A. F., and Leamy, M. J., 2021, "Passive Nonreciprocity in a System of Asymmetrical Rotational Oscillators," Physical Review Applied, 15(3), p. 034005.
- [36] Hussein, M. I., Leamy, M. J., and Ruzzene, M., 2014, "Dynamics of phononic materials and structures: Historical origins, recent progress, and future outlook," Applied Mechanics Reviews, 66(4), p. 040802.
- [37] Trainiti, G., 2018, "Wave propagation in space and time modulated structures," Georgia Institute of Technology.
- [38] Chao, G., 1970, "Parametric amplification of surface acoustic waves," Applied Physics Letters, 16(10), pp. 399-401.